IET The Institution of Engineering and Technology **WILEY**

ORIGINAL RESEARCH

An on-body antenna for control of a wireless prosthesis in the 2.45 GHz industrial scientific and medical frequency band

Remko Proesmans[1] | Kenneth Deprez[2] | Maarten Velghe[2] | Arno Thielens[2]

[1]Department of Electronics and Information Systems, Ghent University-imec, Ghent, Belgium

[2]Department of Information Technology, Ghent University-imec, Ghent, Belgium

Correspondence

Arno Thielens, Department of Information Technology, Ghent University-imec, Technologiepark-Zwijnaarde 126, Ghent B-9052, Belgium.
Email: arno.thielens@ugent.be

Abstract

Electronic prostheses require a communication link to other on-body nodes, for example, for control signal extraction. This link can be made wireless to improve user experience compared to wired solutions. Even though ample on-body communication techniques have been described for wireless body area networks, in prosthetics, the efficiency of wireless links is often neglected, in particular when radio frequency (RF) antennas are used. This work aims to show the benefit of on-body RF antenna design for prosthetics, by developing a dedicated antenna for use in a lower arm prosthesis. Additionally, this work tries to fill a gap in literature, where some antennas for dedicated on-body RF communication are presented, but no antennas specific for communication along the arm exist. To this aim, numerical simulations are performed using a cylindrically layered arm model to design a novel, electrically small, capacitively loaded, meandered, 2.45 GHz monopole antenna. The antenna is fabricated using 3D printed polylactic acid and validated both in a static human arm channel and in a dynamic setting, where the human subject performs various tasks. This antenna outperforms an off-the-shelf printed circuit board (PCB) antenna by 18 dB and a rectangular patch antenna by 4 dB in terms of link budget at a separation distance of 20 cm, both in line of sight and non-LOS path loss experiments. Additionally, while performing four commonplace activities, the average power received increased by 20 dB in an on-body link established between two of our novel antennas rather than two of the PCB antennas. These results will aid in the development of wireless prostheses used by a growing number of amputees.

KEYWORDS
dielectric materials, monopole antennas, radio propagation, radio-frequency antenna measurements, simulation

1 | INTRODUCTION

Typical portable radio frequency (RF) devices are designed in free space. However, the sheer presence of a user near a device impacts its radiation characteristics. This is of particular importance for wearable devices that are used in very close proximity to the human body [1]. For this reason, interest in the human body as a channel for communication, rather than a hindrance of it, has emerged. This principle is the foundation of wireless body area networks (WBANs) [1, 2] and is of great use in prosthetics, as wireless prostheses offer higher user comfort than wired alternatives. On-body wireless propagation has been studied using numerical simulations [3–5], measurement campaigns using on-body antennas [3–8], and theoretical models [9, 10]. Using these results, (dynamic) channel models for on-body RF propagation have been developed [3–8, 11]. Effort has been made to introduce prostheses into the WBAN, but WBAN-specific knowledge has only permeated the control plane of prosthetics [12], with little to no consideration for efficient communication between an on-body node and the prosthesis [13, 14]. Indeed, in the currently predominant configuration of electronic prostheses, they are connected with wearable sensors using a wired connection that protrudes the prosthesis and is carried alongside the arm, see Figure 1. This

State of the Art

This Research
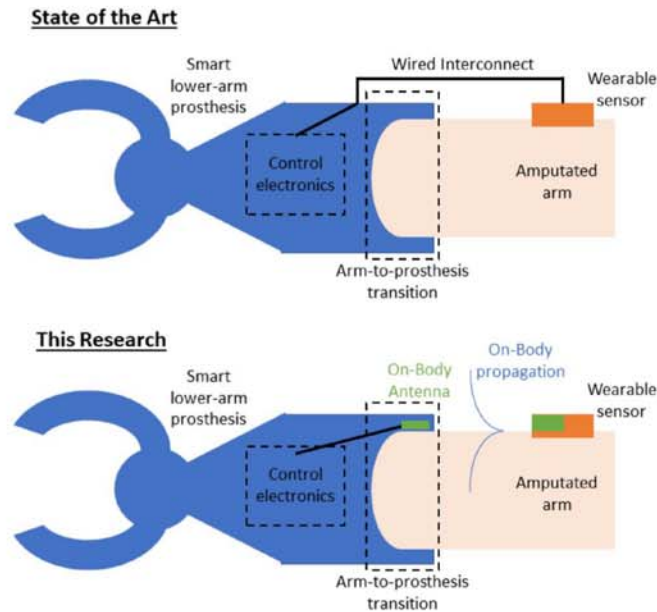
FIGURE 1 Illustration of the goal of the proposed research. The upper figure shows the current state of the art in smart lower arm prostheses, which use wired interconnects to connect a wearable sensor with the prosthesis. We propose the development of the system shown below, where the wires are replaced by an integrated on-body antenna, designed for communication along the arm.

impedes the movements of the patients and causes discomfort. The goal of our work is to replace this wired link by a wireless link using on-body antennas (bottom of Figure 1 in green). In particular, we want to work with an on-body antenna that is integrated in the arm-to-prosthesis transition volume, where a relatively thin section of the prosthesis encloses the arm.

The frequency of interest in this manuscript is the 2.45 GHz industrial, scientific, and medical (ISM) band, given the vast number of wearable sensors that use it. On-body RF communication has been studied in this band [5, 6, 8–10] and compact antennas for on-body RF communication operating in it have been demonstrated [15–17]. An attractive new method to fabricate such antennas is additive manufacturing, which enables the use of lightweight plastic in custom shapes that are difficult or expensive to achieve using more conventional fabrication methods such as printing on circuit boards or injection moulding. 3D printed antennas have been demonstrated in refs. [18–21], using different strategies for applying conductive materials on 3D-printed substrates, such as: using patterned copper tape [18], printed conductive filaments [19], printing of conductive patterns on deformable substrates [20], and spray-coating of 3D-printed substrates [21]. 3D printed antennas are also uniquely suited for integration with a new generation of 3D-printed prostheses [22].

The goal of this work is to introduce efficient RF-WBAN communication into the field of prosthetics. To this aim, we have designed, fabricated, and validated a novel, tunable on-body antenna for integration in a limb prosthesis, more specifically in the arm-to-prosthesis transition section, see Figure 1. The antenna presented in this manuscript differentiates itself from other 3D-printed, vertically polarised on-body

antennas because it is (1) compatible with the prosthesis and the 2.45 GHz ISM band and (2) is designed for the 'on-body' and/or 'along-the-arm' channel in particular. The combination of these two items together with the 3D printing as a fabrication method are the novelties of this paper. The antenna was designed using numerical simulations on a cylindrical phantom mimicking a human arm. The antenna structure is fabricated using 3D printing and selectively brush painted using conductive silver ink or covered by copper tape, which is a relatively cheap and fast prototyping method. Finally, the performance of the antenna is evaluated both in a set of predefined on-body path loss experiments and in a long-form experiment where four dynamic activities are performed by a human subject. These results are important for a growing number of amputees whose quality of life could be improved by enhanced wireless connectivity of their prosthesis.

2 | MATERIALS AND METHODS

This section outlines the design, fabrication, and evaluation methodologies used. First, the design principles employed in this work are supported by theoretical results from literature. Second, the materials used to manufacture the designed antennas are presented, after which the different design workflows are detailed, including simulation parameters. Finally, several measurement strategies that serve to validate the on-body antenna design are explained.

2.1 | On-body propagation of RF electromagnetic fields

The transfer of electromagnetic fields (EMFs) between two antennas located on the surface of the human body at a separation distance (d) is commonly described using a summation of three field terms [10, 23–26]: the quasi-static field, the geometric-optics field, and fields associated with Norton surface wave propagation. At relatively small separation distances, in the so-called near field, the transfer of EMFs between two on-body antennas is dominated by quasi-static EMF-coupling with the electric field strengths exhibiting a $1/d^3$-dependency [24, 25]. In this regime, the two antennas are electromagnetically coupled and cannot be considered as two separate systems. Therefore, a design of such an on-body link would require simultaneous optimisation of the antenna pair.

At relatively large separation distances, the Norton surface wave terms with a $1/d$-dependency on the separation distance in terms of electric field strengths dominate [24]. In this regime, the antennas are decoupled and therefore their parameters can be determined independently. Unlike in free space, where this situation would occur if both antennas are in each other's far-field as defined using the Fraunhofer distance, there is no closed formula that determines this distance on the human body. It was shown experimentally in ref. [24] that at 100 MHz and for $d \approx \lambda_0/2w$ (with λ_0, the wavelength in free space and w the largest dimension of the antenna) more than

80% of the E-field strength on the body was carried by a surface wave, while in ref. [10] a separation distance of λ_0 as limit for the on-body far-field condition was put forward at 2.45 GHz. At this frequency $\lambda_0 = 12.2$ cm, which is smaller than most separation distances on the body that would be targeted in this application.

Therefore, we hypothesise that we can execute an on-body antenna design without considering any potential coupling between two antennas. If an RF antenna is to be used on-body, the most efficient antenna polarisation is found to be normal to the skin surface due to a strong excitation of the Norton surface wave [9, 10]. Hence, we aimed to design an antenna with a dominant polarisation orthogonal to the skin. This polarisation requirement is, however, in contradiction to the need for on-body antennas to be low-profile. This is the main design challenge in creating antennas for this application and is discussed further in Section 2.3.

2.2 | Antenna materials

The antennas in this work are prototyped on a 3D printed polylactic acid (PLA) substrate. The dielectric constant of PLA is determined experimentally by application of the two-line method [27]. This method relies on the difference in S-parameters between transmission lines with different lengths created on the same material. The changes in S-parameters are directly related to the substrate material properties. To this aim, we fabricated two transmission lines on rectangular bricks of solid PLA with 1.5 mm thickness, a width of 2 cm, but with different lengths of 2 and 3 cm respectively, see Figure 2. The transmission lines themselves are made using 4 mm wide copper traces cut from a roll of 3M EMI Shielding Tape 1181 in reference to a ground plane made with the same material. The substrate height of 1.5 mm was chosen to accommodate standard sub-miniature version A (SMA) connectors, of which one was soldered to each side of the transmission lines. These were then connected to a ZNB29 Rhode and Schwarz vector network analyser (VNA) using SMA cables, which recorded the two-port S-parameters of each transmission line in the 2.2–2.7 GHz frequency band using steps of 1 MHz.

The conductive parts of the antennas were fabricated by covering the PLA structures with either the 3M copper tape, similarly to refs. [18, 19], or RS Pro Silver Paint having a volume resistivity of 0.001 $\Omega\cdot$cm, akin to ref. [20], but, as opposed to ref. [20], the radiating element is an intricate 3D structure which must be coated in its proper 3D form, as is the case in ref. [21]. However, in ref. [21], only a parasitic horn is fabricated using 3D printing and conductive coating, not the radiating element. The approach followed in this work thus sets itself apart from the discussed manuscripts [18–21] by combining different aspects of each. The copper tape was cut by hand to fit the necessary surfaces and stuck to the PLA substrate using its adhesive. The silver paint was applied to the PLA using a brush on predefined areas. After application of the paint, the antennas were cured at room temperature for 30 min under a fume hood.

2.3 | Numerical antenna design

Two antennas are designed and manufactured in this work: a standard rectangular patch antenna and a dedicated on-body design, the first serving as a baseline antenna to which the second can be compared.

2.3.1 | Rectangular patch antenna

The first antenna designed in this work is a standard rectangular patch antenna. Its purpose is twofold: (i) confirming the viability of the chosen materials and the measured PLA dielectric constant for antenna prototyping and (ii) evaluating the on-body performance of this antenna type as its form factor makes it an enticing choice for on-body purposes. The design is based on well-established analytical free space formulas [28] and optimised in Keysight ADS (Keysight Technologies). A fixed substrate height of 1.5 mm was again chosen to accommodate standard SMA connectors. The final antenna dimensions will differ slightly from the simulated ones because of inaccuracy in cutting the copper tape and an iterative manufacturing process: it is easiest to first cut the copper too large and subsequently remove strips until an adequate frequency characteristic is achieved.

2.3.2 | Top-loaded, meandered, tunable monopole antenna

The second antenna is specifically designed for on-body use and communication along the arm. Placing an RF antenna on-body is known to shift its resonance frequency and impact the reflection coefficient at that frequency. This must be considered during design. For this reason, the second antenna is entirely designed in the numerical solver Sim4Life (ZMT) on a cylindrically layered arm model derived from literature [29–31], illustrated in Figures 3 and 4. The radius R_{tot} of the entire model is 53.8 mm and follows from the mid-upper arm circumference (MUAC) of the average adult American male [29] through:

$$R_{\text{tot}} = \frac{\text{MUAC}}{2\pi} \qquad (1)$$

The thickness of the fat and skin layer combined, $T_{\text{fat}} + T_{\text{skin}}$, is related to the skinfold thickness T_{sf} of an average adult American male [29]:

$$T_{\text{sf}} = 2\left(T_{\text{fat}} + T_{\text{skin}}\right) \qquad (2)$$

To simulate the antenna in the vicinity of these heterogeneous materials, Sim4Life's finite-difference time-domain solver is used. The design goal is a -10 dB bandwidth of 200 MHz around 2.45 GHz, which is chosen larger than the 2.45 GHz ISM band to allow for some error in manufacturing. The excitation is a 50 Ω voltage source emitting a 1 V Gaussian
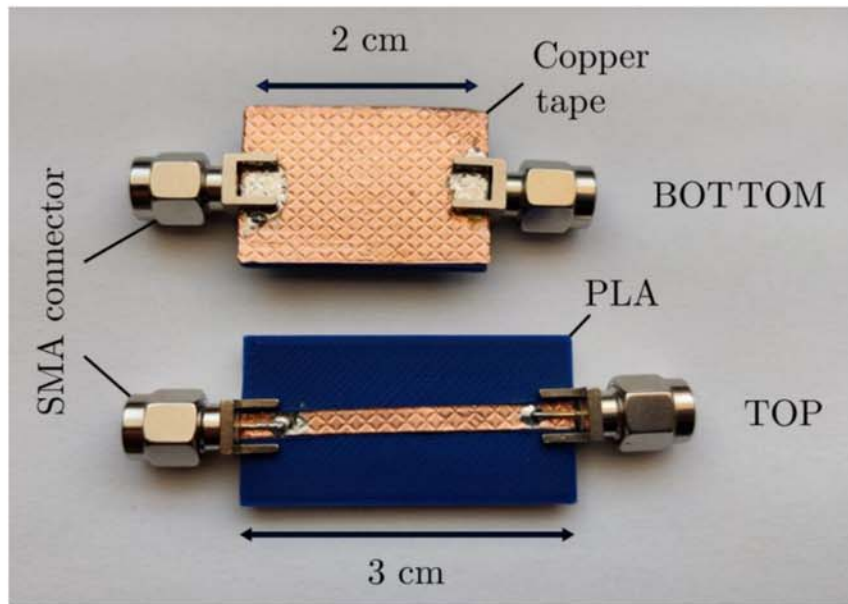
FIGURE 2 Microstrips made using 3D printed polylactic acid (PLA) substrate and copper tape. The substrate thickness is 1.5 mm.
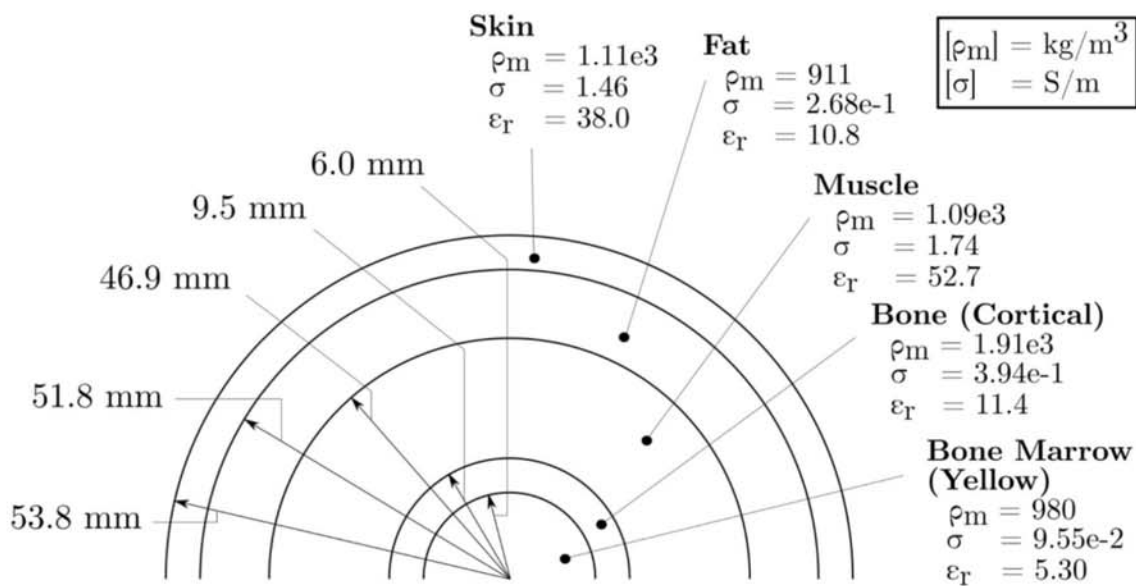

FIGURE 3 Cylindrically layered arm model with dimensions (left) and Sim4Life material parameters (mass density ρ_m, electrical conductivity σ, relative dielectric constant ε_r) at 2.45 GHz (right).

at 2.45 GHz with a bandwidth of 1 GHz for 50 periods. The boundaries of the simulated space are perfectly matched layers. They are padded by 75 mm around the mantle of the arm model and are perfectly fitted to the ends of the model as to mimic an 'infinite' arm. The geometry resolution for the radiating element is 0.25 mm with a 3.45 mm maximum step, 0.1 mm resolution and 1 mm maximum step for the ground plane, while the arm model is placed in an automatic, 'very coarse' sub grid in which Sim4life ensures the stability of the simulation.

The starting point for the antenna design was the quarter wavelength monopole antenna. The advantages of this antenna type is that it is shielded from the human body by its ground plane, which results in stable antenna performance, and that it emits a polarisation orthogonal to the skin, which is hypothesised to excite Norton surface wave propagation more efficiently [9, 10]. However, the disadvantage of this antenna is that it has a relatively large vertical extent (3 cm at 2.45 GHz), whereas in wearable applications, it is preferred to minimise the height of the antenna to increase comfort of the person wearing the antenna. In ref. [9], for example, a planar inverted F-antenna with a height of 4 mm is employed, at the cost of polarisation purity. The low-profile requirement is, however, mitigated when specifically considering integration in prostheses, which commonly have some vertical extent relative to the skin. Exploiting this freedom thus allows for a purer normal field excitation than general on-body antennas typically achieve. In order to reduce the footprint of the monopole antenna, we used a three-dimensional meandering technique shown in Figure 4b.
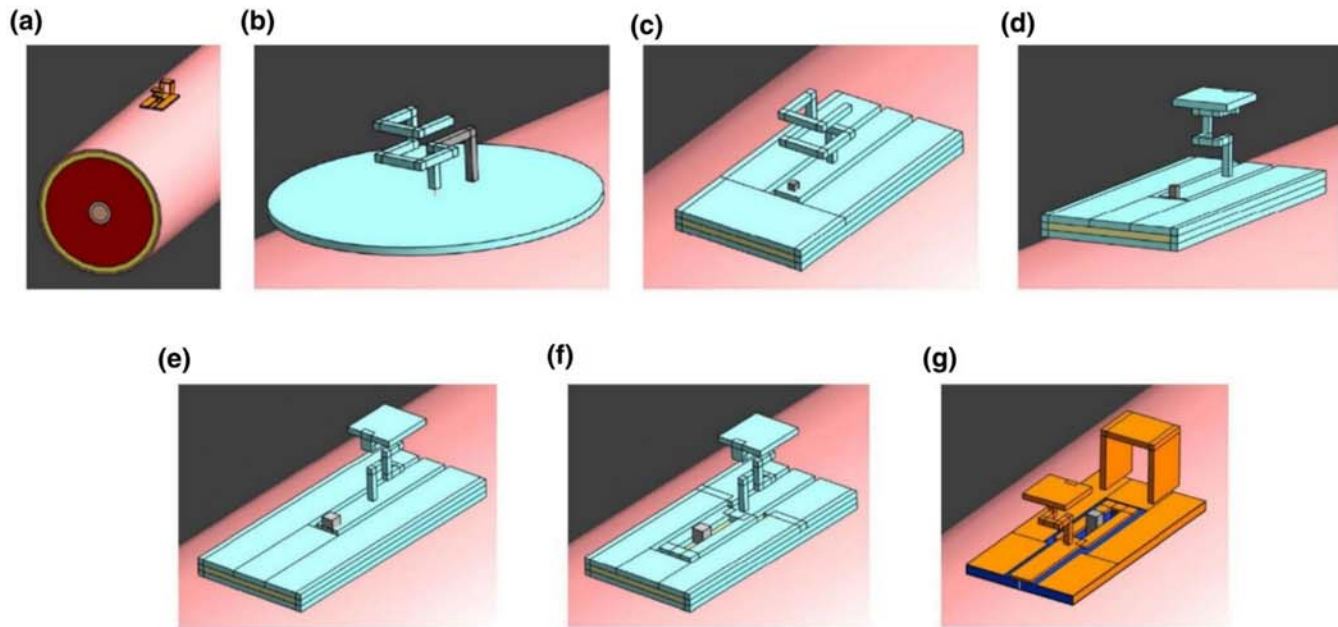
FIGURE 4 Progression of the loaded, meandered monopole antenna design, simulated on the arm model. The blue colour indicates PEC material in the S4L simulation, yellow or dark blue is used for substrate dielectrics, grey for shorts to ground for matching purposes, orange for copper. (a) Example antenna on the arm model of Figure 2. (b) Meandered monopole with IFA-like matching stub, indicating by the grey colour. (c) Meandered monopole with matching integrated in the ground plane. (d) Meandered loaded monopole. (e) Reversed meandered loaded monopole. (f) Reversed meandered loaded monopole, tunable version. (g) Final design, tunable reversed meandered loaded monopole with director. IFA, inverted F-antenna; PEC, perfect electric conducting.

By turning the meander bends back on themselves instead of twisting the antenna like a helix, horizontal currents partly counteract each other, further mitigating the degradation in polarisation. Meandering the antenna is however detrimental to mismatch efficiency. For this reason, a matching stub is added, indicated in grey Figure 4b. This technique is commonly used to match an inverted-L antenna, turning it into an inverted-F antenna (IFA). The light blue colour indicates the use of perfect electric conducting (PEC) material in these initial design stages. A first improvement of the design is shown in Figure 4c and implements feeding using a planar microstrip, avoiding the use of a bottom-feed. It was found that extending the feed line past the radiating element and shorting to ground is a good replacement of the IFA-like stub, providing an effective degree of freedom for matching while simplifying the 3D structure of the antenna. The ground plane wraps around a PLA substrate. The next design iteration shown in Figure 4d makes use of capacitive top loading to increase bandwidth by adding a rectangular conductive segment to the top of the antenna. A similar approach using a conductive disc as top load was followed in ref. [32]. The top load in part adds to the resonant length of the antenna, making the meander branches in Figure 4d shorter than in Figure 4c. Afterwards, the radiating element is rotated 180° as this was found to increase directivity, see Figure 4e. Directivity is preferable because the antenna is meant for integration in prostheses: there is no use in radiating towards the missing limb. In Figure 4f, a mechanically tunable impedance matching is introduced: a slot is made in the ground plane in which the short can be moved back and forth. Lastly, a rectangular arch was added, see Figure 4g, which functions as a parasitic director without increasing the physical dimensions of the antenna. In this last design step, the PEC material is also switched for copper. Note that the entire antenna is rotated 180° between Figure 4f,g to better show the entirety of the antenna.

2.4 | Antenna and channel measurement

Multiple measurements and experiments are performed to characterise and evaluate the antenna types. These range from performing VNA measurements to show proper antenna resonance, to evaluating the antennas in dynamic, real-life scenarios.

2.4.1 | Measurement hardware and conditions

For all antenna S-parameter measurements, the same VNA as for material characterisation is used. Channel measurements, on the other hand, are performed with Particle Argon microcontrollers. This board is built around an Espressif ESP32 module for Wi-Fi capabilities and a Nordic nRF52840 enabling Bluetooth Low Energy (BLE) connectivity. The BLE stack is supported by an internal printed circuit board (PCB) antenna and a U.FL connector for use with an external antenna. Switching between the two is done in software. Figure 5 shows the Argon Particle PCB and the dimensions of its internal PCB antenna. This is a planar meandered IFA [28], which during the measurements was always worn parallel to the skin. The main
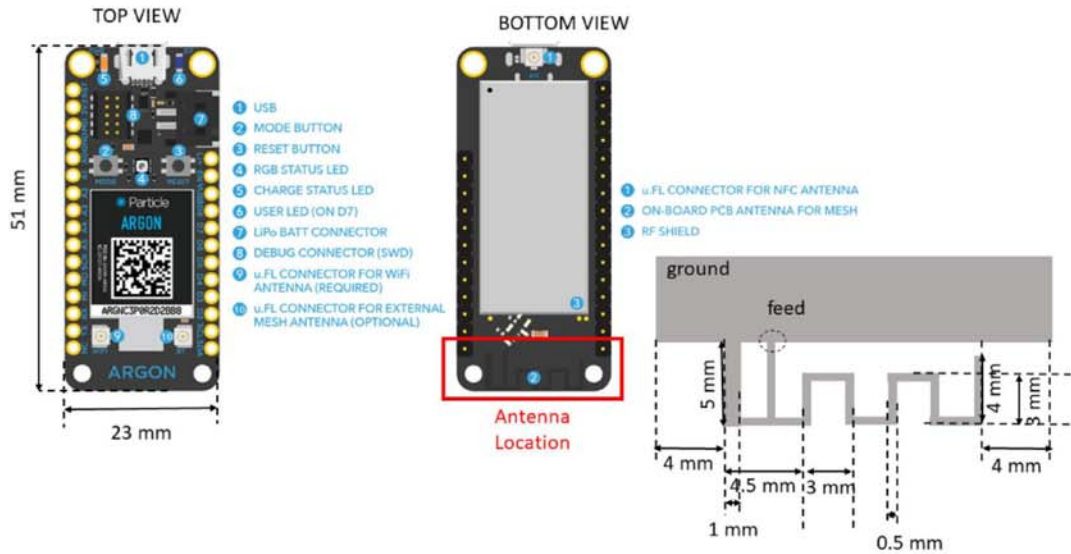
FIGURE 5 Argon Particle board with dimensions and antenna dimensions. *Source*: https://docs.particle.io/reference/datasheets/wi-fi/argon-datasheet/. Accessed 16 August 2022.

polarisation emitted by this antenna is presumably parallel to the skin as well.

The following experiments are performed in different environments, on different persons. Person 1 (P1) is a 23-year-old male, characterised by a MUAC of 25 cm, Person 2 (P2) is a 58-year-old male with a MUAC of 33 cm. Environment 1 (E1) is a low-interference basement, Environment 2 (E2) a spacious living room, Environment 3 (E3) close quarters in a first-floor studio. During all experiments, RF-EMF exposure remains well below ICNIRP guidelines [33] and national legislation.

2.4.2 | Determination of patch antenna radiation efficiency

The choice of PLA material and fixed substrate height constrains the radiation efficiency η_{rad} of the patch antennas. Hence, this parameter is determined and accounted for in upcoming experiments. It is calculated as:

$$\eta_{\mathrm{rad}} = G/D \tag{3}$$

with G the gain and D the directivity. Note that G does not contain the mismatch efficiency in this definition.

For D, the average of the simulated values returned by ADS and Sim4Life is used. The gain G is derived by facing the three patch antennas pairwise towards each other at a distance of 60 cm while surrounded by pyramidal microwave absorbing foams and measuring the S-parameters using the VNA with a 1 MHz step over a 500 MHz bandwidth. For each of these three measurements, the following adaptation of the Friis formula holds:

$$|S_{ij}|^2 = \left(1 - |S_{ii}|^2\right) G_i L_0^{-1} \left(1 - |S_{jj}|^2\right) G_j \tag{4}$$

with $i,j \in \{1,2,3\}$, $i \neq j$, S_{ij} the transmission S-parameter measured between antennas i and j, $G_{i/j}$ the gain of antennas i/j, respectively, and L_0 the path loss defined as:

$$L_0 = \left(\frac{4\pi r}{\lambda}\right)^2 \tag{5}$$

where r is the distance between the two nodes and λ the wavelength at 2.45 GHz. The resulting system of three equations is solved for the gains of the three patch antennas G_1, G_2, and G_3.

2.4.3 | On-body characterisation of top-loaded, meandered, tunable monopole antenna

S-parameter measurements of the on-body antenna are performed on Person 1 in Environment 1. The antenna is connected to the VNA through an SMA cable and fixed to the forearm using a combination of tape and rubber bands. To test the effect of the director, two of such antennas are attached in a similar way, facing each other in a line of sight (LOS) configuration over the forearm at a distance of 20 cm, at which point a measurement with and without the directors is performed. For the measurement with directors, these are set in place on the ground planes without fixing, so that they can be easily removed for the measurement without directors immediately afterwards, without influencing any other measurement conditions.

2.4.4 | Static on-body measurements

A first set of experiments derives the path loss for different on-body channels between receiver (RX) and transmitter (TX), shown in Figure 6, using pairs of the same antenna type. The over-the-arm (OTA) paths in Figure 6a,b represent
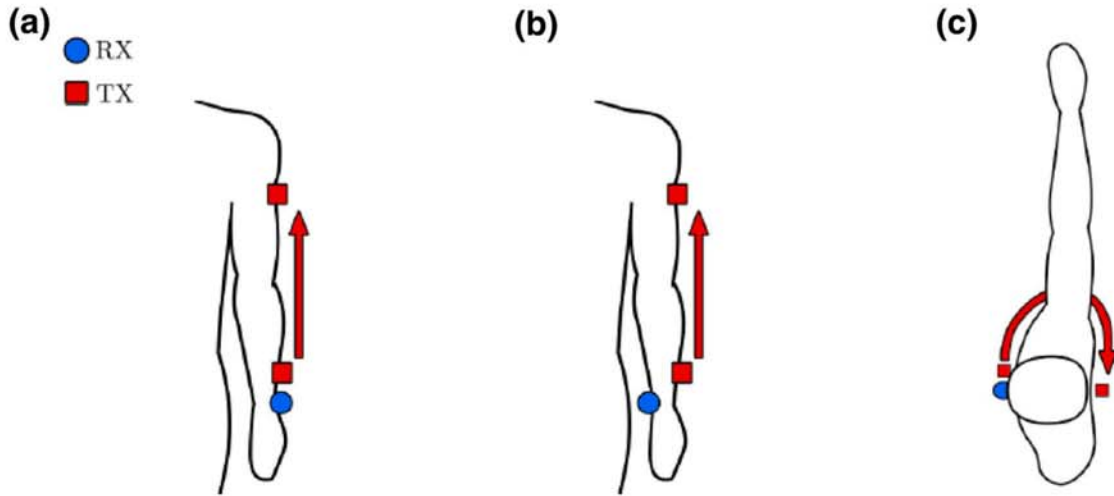
FIGURE 6 Evaluated propagation paths. (a) Over-the-arm line of sight (LOS) path. (b) Over-the-arm non-LOS path. (c) Around-the-body path.

possible communication links between a lower arm prosthesis and an external node elsewhere on the arm. The around-the-body path in Figure 6c will show the benefit of on-body antenna design in an amplified way. Measurements were done with Person 1 in Environment 1 and Environment 2, and with Person 2 in Environment 2. The experiments are performed as follows. Two Particle Argon micro-controllers exchange Bluetooth advertisement packets transmitted at 0 dBm, either using the internal or an external BLE antenna, from which the received power P_r is extracted. At each distance step along the channel, 30 such values are averaged and a path loss model is least square fitted to the resulting data points:

$$P_r(d) = P_0 - 10.n.\log_{10}\left(\frac{d}{d_0}\right) + N\left(0, \sigma_p^2\right) \qquad (6)$$

with n the path loss exponent, P_0 the received power at reference distance 10 cm, and $N\left(0, \sigma_p^2\right)$ the lognormal variance. This is repeated for a pair of rectangular patch antennas, a pair of meandered monopoles and the internal PCB antennas of the Particle Argon boards. For the pair of meandered monopoles, an additional free space measurement is performed to evaluate to what extent the on-body path loss approximates free space path loss.

2.4.5 | Dynamic on-body measurements

In a second set of experiments, P1 wears the antennas in E3 for multiple hours while performing different tasks to characterise communication link stability. The tasks performed are playing the piano, exercising (push-ups, weight lifting), sitting idle (extended periods of no movement in between occasional change of sitting position) and cleaning (vacuuming, moving between rooms). Particle Argon microcontrollers are again


FIGURE 7 Example of configuration during dynamic measurements.

used to exchange BLE advertisements from which P_r samples are extracted, with the RX at the same location as in Figure 6a and the TX in a LOS configuration at a fixed distance of 20 cm when the arm is stretched. Figure 7 shows an illustration of the worn system. The RX then relays the received power values through Wi-Fi to a remote laptop running a Python HTTP server. This server received, on average, 1.8 P_r samples per second from the RX. The lognormal mean $P_{r,\mathrm{avg}}$ and lognormal standard deviation σ_{P_r} are calculated over a running 30 s window, with σ_{P_r} defined through:

$$\sigma_{P_r}^2 = \frac{1}{N-1} \sum_{i=1}^{N} \left(P_{r,i}[\mathrm{dB}] - P_{r,\mathrm{avg}}[\mathrm{dB}]\right)^2 \qquad (7)$$

with N the number of samples within the given 30 s window and $P_{r,i}$ the ith sample in the window. The information in these metrics is condensed by empirical cumulative distribution functions (CDFs). This experiment is only repeated for the
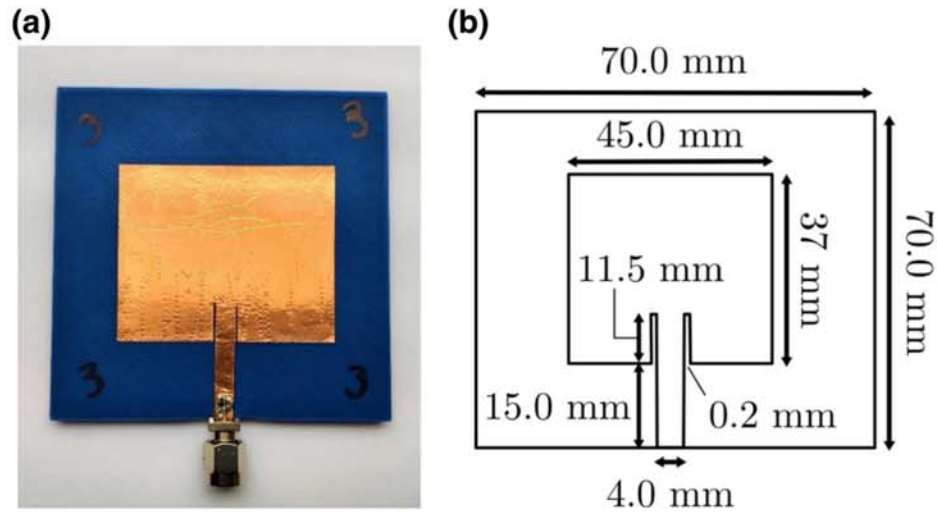
FIGURE 8 2.45 GHz rectangular patch antenna made with copper tape on polylactic acid (PLA) substrate. (a) Prototyped rectangular patch antenna and (b) Simulated dimensions, the substrate thickness is 1.5 mm.

meandered antennas and the PCB antennas, as the rigid patch antennas are not suitable for wearing during dynamic tasks.

3 | RESULTS

This section presents the results of the design and manufacturing process as well as the validation experiments. Single antenna VNA measurements are briefly discussed to show the functioning of the antennas, an in-depth discussion of the static and dynamic validation experiments described in Sections 2.4.4 and 2.4.5 is given in Section 4.

3.1 | Dielectric characteristics of PLA

The dielectric constant of PLA was determined experimentally by application of the two-line method [27] and was found to be 2.7 at 2.45 GHz, with a loss tangent of 0.009. For comparison, [19, 34] respectively report a dielectric constant of 2.54 and 2.75, and a loss tangent of 0.007 and 0.011.

3.2 | Patch antennas

The final patch antenna can be seen in Figure 8a with the exact simulated dimensions in Figure 8b. Three rectangular patch antennas were fabricated, their free space frequency characteristics are given in Figure 9. The measured bandwidth is 61–99 MHz, compared to 45 MHz in simulation. The resonance frequency was measured to be 2.438–2.444 GHz, compared to 2.444 GHz in simulation. The measured radiation efficiency is found to be 54.3%–62.0%. To account for this low efficiency, received power values with the patch antenna presented in the following experiments are incremented by 2.7 dB. This way, the corrected performance of the patch antennas can be viewed as a 'best-case' performance.
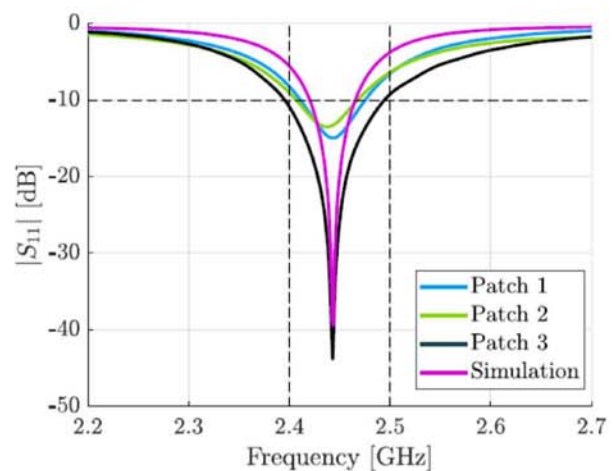
FIGURE 9 Measured and simulated frequency characteristics of the patch antennas.

3.3 | Top-loaded, meandered, tunable monopole antenna

The final antenna is shown in Figure 10, with dimensions in Figure 11. It is a monopole antenna, given the efficiency of normally polarised fields as discussed in the introduction, meandered in 3D to decrease its height. A 50 Ω match is achieved by an extension of the feed line shorted to ground. The short is movable for mechanical tuning, which can negate manufacturing errors and allows for subject-specific impedance tuning. Capacitive top loading is applied to improve bandwidth and further decrease vertical size. The rectangular arch is a parasitic director and was found to improve on-body S_{12} by 1.2 dB when a pair of antennas is separated by 20 cm in a LOS OTA configuration. The antenna's bounding box is 20.0 mm by 40.0 mm by 13.5 mm, making it suitable for integration in prostheses as shown in Figure 1.

FIGURE 10 On-body antenna prototype made with 3D printed polylactic acid (PLA), copper tape and RS Pro Silver Paint.
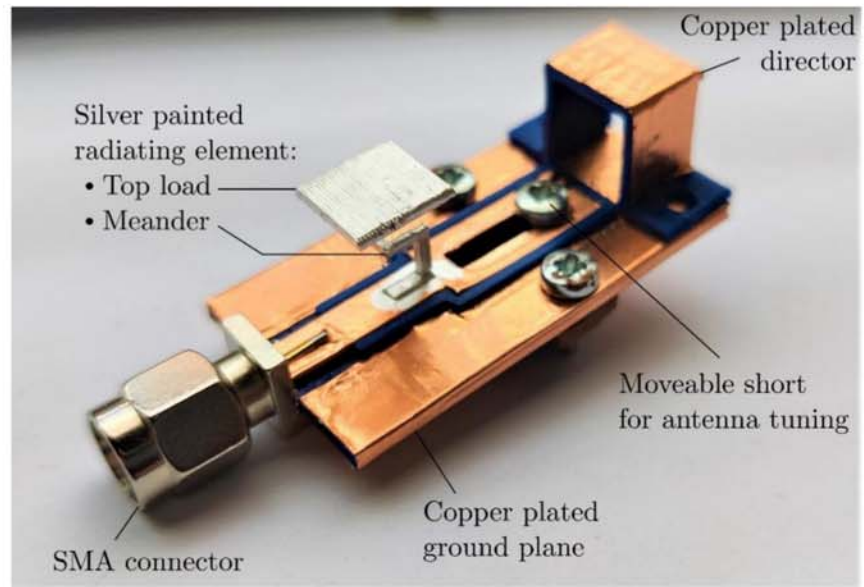

Figure 12 shows measured on-body S_{11} characteristics for a single tunable antenna. The resonance frequency can be shifted from 2.41 to 2.47 GHz, with the best possible match at 2.45 GHz being an S_{11} of −30 dB. The inset Smith chart in the figure characterises the tuning mechanism, which provides matching of −12 dB down to −30 dB at the centre frequency.

3.4 | Static path loss measurements

The results of the path loss experiments are shown in Figure 13 with fitting parameters given in Table 1, which also shows fitting parameters for similar experiments in literature. The results are discussed in Section 4.2.

3.5 | Dynamic experiments

The measurements for the second set of experiments are shown in Figure 14a. The vertical axis shows the received power in the studied LOS OTA scenario using the meander designed in this work (blue) and the on-board PCB antenna (green), for four different activities. The figure demonstrates that the meandered antenna results in a more stable (less variation) and more efficient link (higher received power for the same emitted power). This is further quantified in Figure 14b,c, which show CDFs of the received power during the measurements for the meandered monopole antenna and the PCB antenna respectively. Figure 14d,e, on the other hand, show the standard variations on the same measurements.

4 | DISCUSSION

Here, the final on-body design is briefly considered. Then, the results from the static and dynamic validation experiments, see Sections 3.4 and 3.5, are discussed.

4.1 | Top-loaded, meandered, tunable monopole antenna

The antenna's bounding box is $20.0 \times 40.0 \times 13.5$ mm³, making it suitable for integration in prostheses, as envisioned in Figure 1. It is possible to design smaller on-body antennas in the 2.4 GHz ISM band, for example, the antenna of ref. [17] is $26 \times 26 \times 4$ mm³. However, this reduces the radiation efficiency: for example, our simulated maximum on-body gain is 3.6 dBi, whereas the overall maximum (not on-body) gain of the antenna in ref. [17] is −0.6 dBi. At higher frequencies, it is possible to achieve higher efficiencies and on-body gains with smaller antennas as demonstrated in refs. [15, 16]. On-body gains and efficiencies depend on the body's dielectric parameters and the coupling of RF EMF fields to the body, so there is not necessarily a one on one relationship between frequency and potential achievable on-body gain and efficiency.

4.2 | Static path loss measurements

The results of the path loss experiments are shown in Figure 13 and Table 1. The meandered monopole outperforms the PCB antenna and the corrected patch antenna (with performance enhanced by 2.7 dB) by respectively 15–28 and 4–9 dB. In terms of path loss exponent n, the patch antenna performs best in the LOS OTA scenarios: the path loss exponent ranges from 1.7 to 1.8 for the patch antenna, in comparison to 2.4–3.2 for the PCB antenna and 2.1–2.3 for the meandered antenna. However, for realistic distances on the body ($d \leq 2$ m) this does not compensate the lower mean received power level compared to the meandered monopole. Similarity is noted between the LOS, P1, E2 experiment with the meandered monopole in this work and the 2 GHz monopole in ref. [8] with regards to all quantities mentioned in Table 1. In non-LOS OTA conditions, all antennas show relatively high path losses at reference distance P_0, at least 8 dB
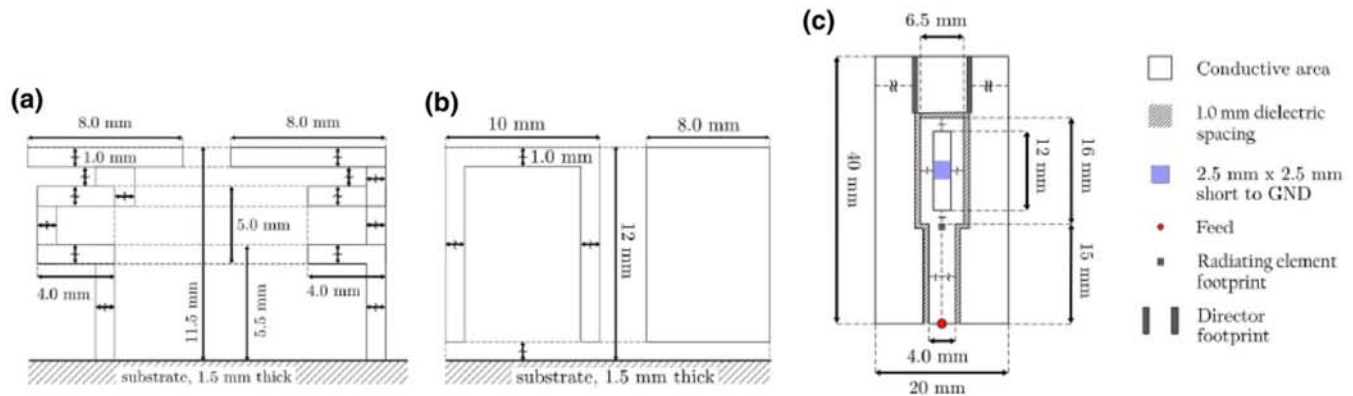
FIGURE 11 Dimensions of the on-body antenna design. (a) Radiating element. (b) Director. (c) Ground plane with signal trace.
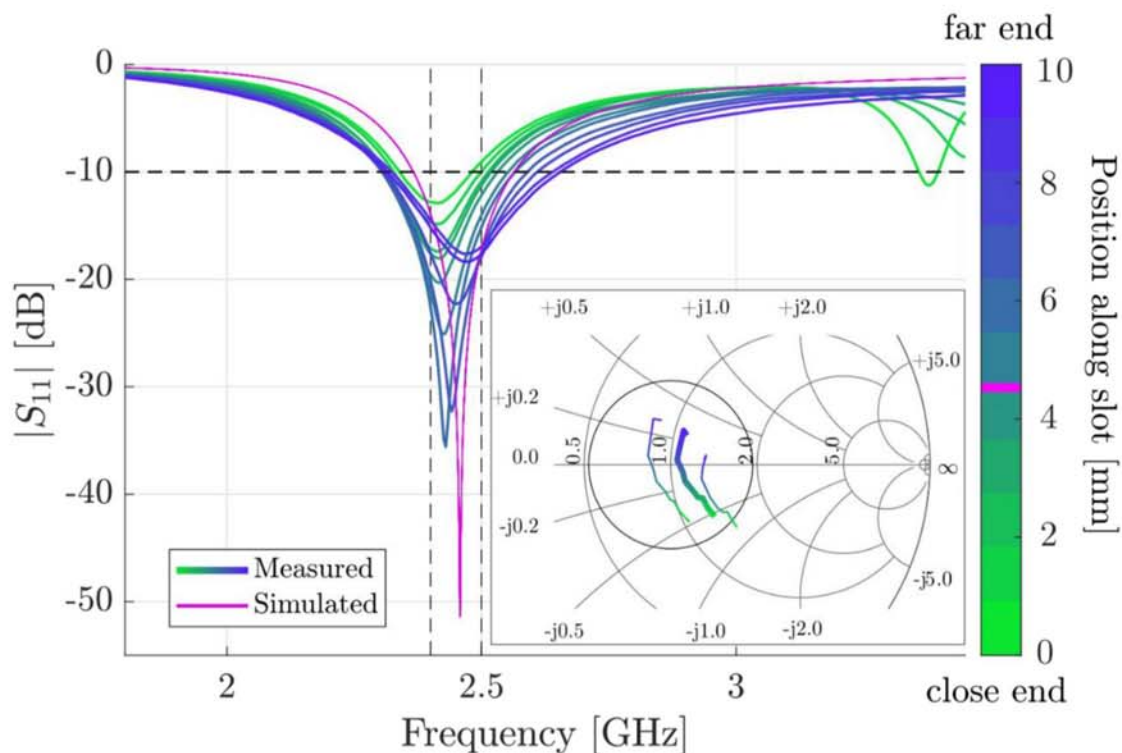

FIGURE 12 On-body frequency characteristics of the meandered monopole. The 'close end' of the slot is near the radiating element, the other end is the 'far end'. The lines in the Smith chart correspond to 2.40, 2.45, and 2.50 GHz from left to right.

lower than in the LOS OTA experiments. Path loss exponents in non-LOS are lower than those found in the equivalent LOS scenarios. The PCB antenna in this work provides the lowest received power levels overall and results in a higher variance, similarly to the PCB antenna of ref. [8]. We attribute this to the polarisation tangential to the human body used by this antenna. Reusens and Roelens [35, 36] both use tangential dipoles, which translates to a similar path loss performance, worse than the normally orientated antennas in this work and in ref. [8]. The integrated IFA antenna of ref. [37] also performs poorly, similar to the BLE PCB antenna of the Particle Argon evaluated in this work.

Figure 13a shows that, in a LOS scenario, the wearer has no significant impact on received power given the standard deviation on the data samples, that is, the path losses at the reference distance of 10 cm show <2 dB difference from P1 to P2 in the same experiment, and the differences in the path loss exponents are smaller than 0.2 on values ranging from 1.7 to 3.2. Similar results were also obtained in ref. [37].

Figure 13b on the other hand shows that the environment impacts communication performance when using the PCB antennas or the patch antenna with changes in $P_0 \leq 6$ dB and changes in n of 0.2 and 0.6, for the patch and PCB antenna, respectively, while for the link between the meandered antennas, the parameters remain stable over the two tested environments with no change in P_0 and a change of 0.1 in n, see Table 1. Figure 13c shows that in non-LOS conditions all antennas show poorer performance compared to the equivalent LOS scenario.
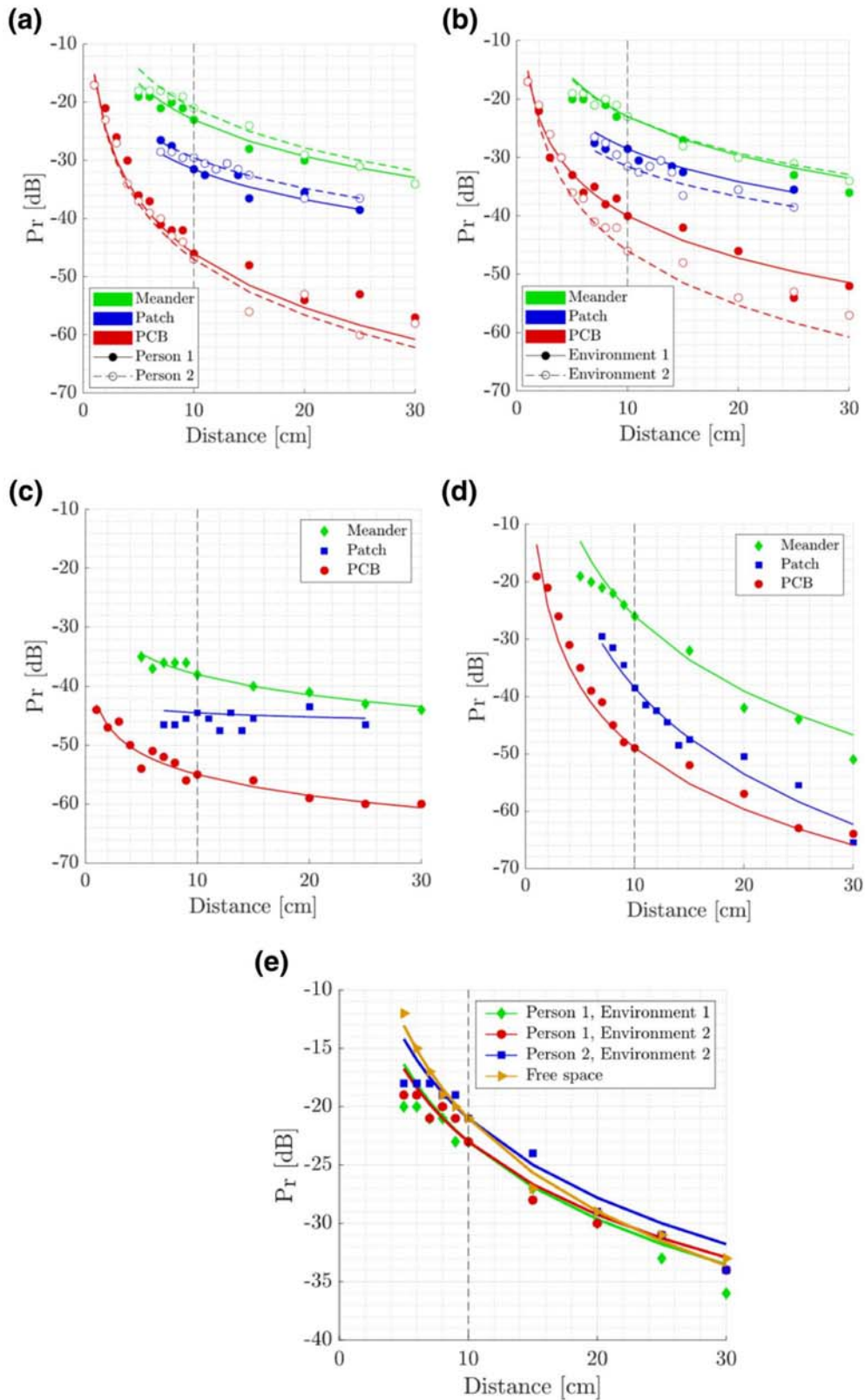
FIGURE 13 Path loss experiments with $d_0 = 10$ cm, indicated by the vertical dashed line. The markers indicate the lognormal mean over 30 measurements of the received power at certain distances, while the curves indicate the fitted path loss models following Equation (6). (a) Line of sight (LOS) propagation path compared for different wearers of the antennas in the same environment. (b) LOS propagation path compared for a single wearer in different environments. (c) Non-LOS propagation path. (d) Around-the-body propagation path. (e) Final comparison for the meandered antenna measured on-body and in free space.

TABLE 1 Fitting parameters for the path loss model in Equation (6) for all evaluated antenna types in this work and comparable sources from literature for a reference distance $d_0 = 10$ cm

		P_0 [dB]	n	σ_P [dB]
LOS OTA P1, E1	Meander	−23	2.21	1.14
	Patch antenna	−28	1.87	1.98
	PCB antenna	−40	2.39	2.18
LOS OTA P1, E2	Meander	−23	2.08	1.23
	Patch antenna	−31	1.73	2.54
	PCB antenna	−46	3.09	2.30
LOS OTA P2 E2	Meander	−21	2.26	1.65
	Patch antenna	−29	1.75	2.34
	PCB antenna	−47	3.17	3.61
NLOS OTA P1, E1	Meander	−38	1.15	2.83
	Patch antenna	−44	0.234	1.90
	PCB antenna	−55	1.18	3.16
ATB P1, E1	Meander	−26	4.34	2.17
	Patch antenna	−38	5.00	2.44
	PCB antenna	−49	3.55	2.71
LOS free space	Meander	−21	2.65	0.66
LOS OTA [35]	2.45 GHz dipole	[−41, −32]	[3.23, 3.35]	/
LOS OTA [36]	2.45 GHz dipole	[−50, −30]	[2.5, 4.0]	/
LOS OTA [8]	2 GHz monopole	−19	2.0	1.3
	2.4 GHz PCB antenna	−62	1.7	1.8

Abbreviations: ATB, around-the-body; LOS, line of sight; NLOS, non-LOS; OTA, over-the-arm; PCB, printed circuit board.

The meandered antenna designed in this work, outperforms the other options in the studied range of communication distances, mainly due to a P_0 that is 6 and 17 dB higher than the patch and PCB antennas respectively. Figure 13d demonstrates that even though the meander was not designed for an around the body scenario specifically, it does perform better than the alternatives, with a P_0 that is much closer to the values found in LOS (3 dB difference) for the same person than for the other antennas, which show degradation in P_0 of 7–10 and 3–9 dB for the patch and PCB antennas respectively. Lastly, Figure 13e shows that the free space path loss for the meandered antennas is similar to the on-body path loss at the targeted separation distances. However, as Table 1 shows, the path-loss exponent n is higher in free space than on the body. This seems to be a consequence of the on-body P_r values for very small separation distances being notably lower than in the free space case. When comparing for example, the free space data points with those of the Person 2, Environment 2 experiment: starting from a separation distance of 7 cm, the datapoints are almost identical. It is thus concluded that the meandered monopole antenna designed

in this work performs equally well on-body as it does in free space, when neglecting unpractically small separation distances.

4.3 | Dynamic experiments

Figure 14b,c show that the difference between tasks in terms of average received power is limited when the same antenna is used: the median of the windowed average received power varies by only 3 dB for both antennas. However, the difference in median compared between antennas per task is much larger at around 20 dB (compare Figure 14b,c). The slope of the CDF curves also differs when comparing antennas: for the PCB antenna, the 10–90 percentile range encompasses 21 dB, for the meandered monopole this is only 8.0 dB. Using the meandered monopole antennas for communication thus results in a higher and more consistent received power level.

The variance on the samples is also improved, as indicated by the cumulative distributions in Figure 14d,e. A clear separation is seen between the more static tasks, playing the piano and idling, and the other two, more dynamic tasks: the median windowed standard deviation differs by 2.9 dB between static and dynamic tasks for the PCB antenna and by 1.0 dB for the meandered monopole. The median standard deviation values per task are 2.0 and 4.0 dB higher for static tasks (piano and idle) and dynamic tasks (exercise and cleaning), respectively, when comparing antennas. Lastly, for the PCB antenna, the 10–90 percentile range of the standard deviation spans 2.0–6.0 dB for static tasks and 3.7–8.0 dB for dynamic tasks, while for the meandered monopole this is about 1.0 and 2.3 dB respectively.

5 | CONCLUSIONS

In this work, two resonant antennas for the 2.45 GHz ISM band were designed and prototyped using 3D printed PLA, 3M EMI shielding tape and RS Pro silver paint, a fast and cheap prototyping method combining different aspects of similar antennas from literature in a novel way. The dielectric constant of the used PLA was determined to be 2.7, with a loss tangent of 0.009. Path loss experiments have shown that off-the-shelf PCB antennas perform poorly on-body, relative to even a standard rectangular patch antenna.

In a human arm channel, an improvement of at least 10 dB can be expected, making the rectangular patch antenna a good choice for on-body communication, considering its low profile. A specialised on-body design with normal polarisation improves performance even further, resulting in at least 15 dB gain in received power compared to the PCB antenna. Dynamic experiments show that the median received power improves by about 20 dB when using the on-body antenna design versus the PCB antenna. The median standard deviations on the received power are 2 and 4 dB higher when using the PCB antennas instead of the meandered on-body antennas, in static and dynamic activities, respectively, indicating that a more stable communication link is established using the meandered
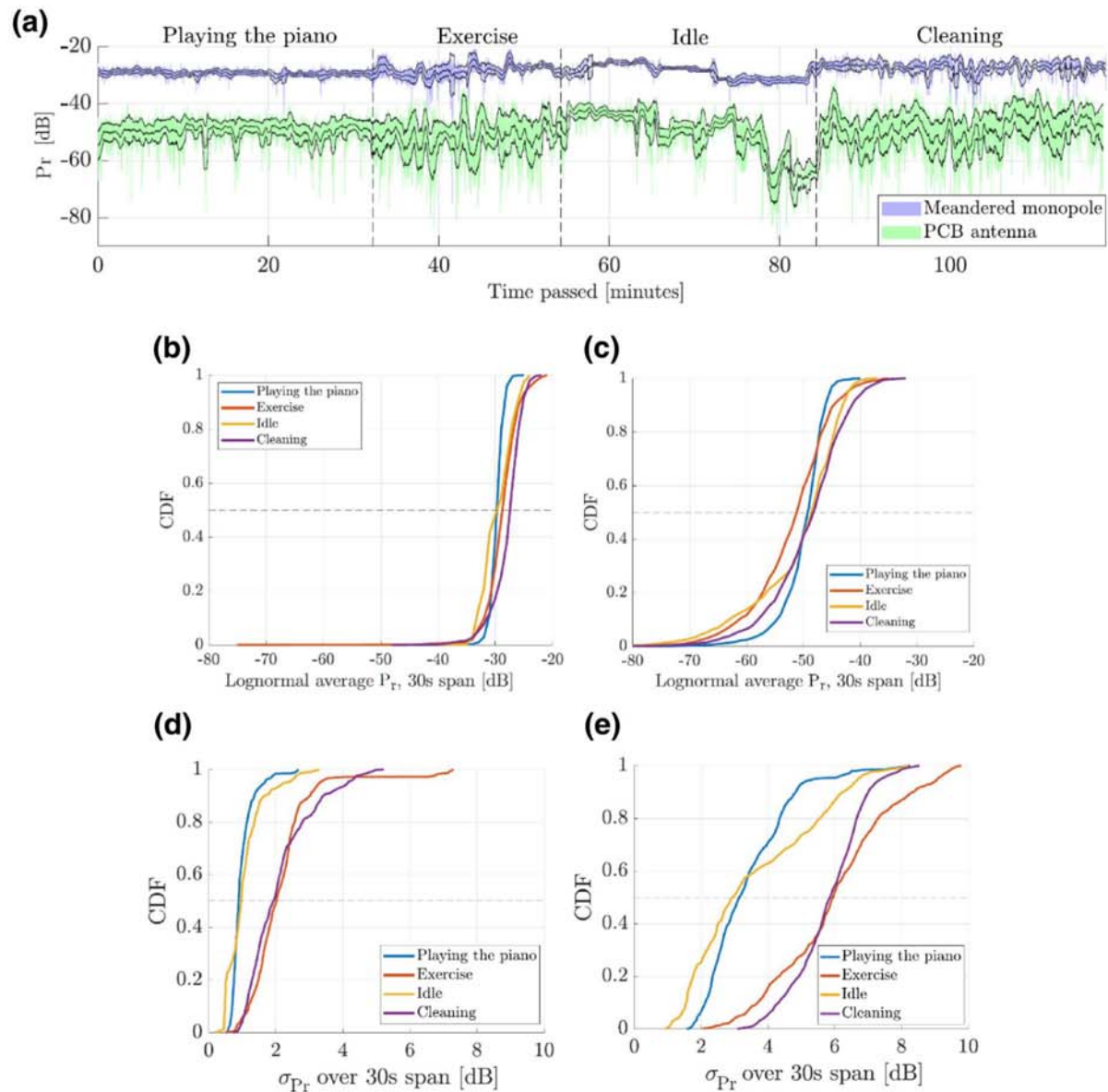
FIGURE 14 Data from the long-form experiment. (a) Received P_r values with 1.8 Hz sample frequency (blue and green curves). The 30 s mean and a 2σ interval around it are indicated by the black lines. (b) CDF of 30 s lognormal average, meandered monopole antenna. (c) CDF of 30 s lognormal average, PCB antenna. (d) CDF of 30 s lognormal standard deviation, meandered monopole antenna. (e) CDF of 30 s lognormal standard deviation, PCB antenna. CDF, cumulative distribution function; PCB, printed circuit board.

antennas. These results were made possible by an on-body antenna design exploiting the vertical dimension, while maintaining a constrained height of 13.5 mm to facilitate integration in prostheses. In future work, we aim to integrate the antenna in a 3D-printable prosthetic and evaluate the subsequent effect on on-body performance. Additionally, a comparison to popular on-body antenna types such as the planar inverted-F antenna is to be performed.

AUTHOR CONTRIBUTIONS

Remko Proesmans: Conceptualisation; Formal analysis; Investigation; Methodology; Validation; Visualisation; Writing – original draft; Writing – review & editing. **Kenneth Deprez**: Investigation; Methodology; Supervision; Writing – review & editing. **Maarten Velghe**: Methodology; Project administration; Supervision; Writing – review & editing. **Arno Thielens**: Conceptualisation; Methodology; Visualisation; Writing – review & editing.

ACKNOWLEDGEMENT

CONFLICT OF INTEREST

The authors report no conflicts of interests.

DATA AVAILABILITY STATEMENT

The data that support the findings of this study are available from the corresponding author upon reasonable request.

ORCID

Arno Thielens https://orcid.org/0000-0002-8089-6382

REFERENCES

1. Chen, M., et al.: Body area networks: a survey. Mobile Network. Appl. 16(2), 171–193 (2011). https://doi.org/10.1007/s11036-010-0260-8
2. Ghamari, M., et al.: A survey on wireless body area networks for eHealthcare systems in residential environments. Sensors. 16(6), 831 (2016). https://doi.org/10.3390/s16060831
3. Aminzadeh, R., et al.: On-body calibration and measurements using personal radiofrequency exposimeters in indoor diffuse and specular environments. Bioelectromagnetics. 37(5), 298–309 (2016). https://doi.org/10.1002/bem.21975
4. Marinova, M., et al.: Diversity performance of off-body MB-OFDM UWB-MIMO. IEEE Trans. Antenn. Propag. 63(7), 3187–3197 (2015). https://doi.org/10.1109/tap.2015.2422353
5. Reusens, E., et al.: Characterization of on-body communication channel and energy efficient topology design for wireless body area networks. IEEE Trans. Inf. Technol. Biomed. 13(6), 933–945 (2009). https://doi.org/10.1109/titb.2009.2033054
6. Alomainy, A., et al.: Statistical analysis and performance evaluation for on-body radio propagation with microstrip patch antennas. IEEE Trans. Antenn. Propag. 55(1), 245–248 (2007). https://doi.org/10.1109/tap.2006.888462
7. van Roy, S., et al.: Dynamic channel modeling for multi-sensor body area networks. IEEE Trans. Antenn. Propag. 61(4), 2200–2208 (2013). https://doi.org/10.1109/tap.2012.2231917
8. Thielens, A., et al.: A comparative study of on-body radio-frequency links in the 420 MHz–2.4 GHz range. Sensors. 18(12), 4165 (2018). https://doi.org/10.3390/s18124165
9. Ivsic, B., et al.: An insight into creeping electromagnetic waves around the human body. Wireless Commun. Mobile Comput. 2017, 1–8 (2017). https://doi.org/10.1155/2017/2510196
10. Grimm, M., Manteuffel, D.: Norton surface waves in the scope of body area networks. IEEE Trans. Antenn. Propag. 62(5), 2616–2623 (2014). https://doi.org/10.1109/tap.2014.2307347
11. Molisch, A.F.: Ultrawideband propagation channels-theory, measurement, and modeling. IEEE Trans. Veh. Technol. 54(5), 1528–1545 (2005). https://doi.org/10.1109/tvt.2005.856194
12. Saleh, A., et al.: A wireless body area network architecture for a prosthetic arm. In: 7th International Congress on Ultra Modern Telecommunications and Control Systems and Workshops (ICUMT), pp. 275–280 (2015)
13. Salminger, S., et al.: Long-term implant of intramuscular sensors and nerve transfers for wireless control of robotic arms in above-elbow amputees. Sci. Robot. 4(32) (2019). https://doi.org/10.1126/scirobotics.aaw6306
14. Bergamini, L., et al.: WiseTOP: a quality of service-aware low power acquisition and wireless communication platform for prosthesis control. In: 26th IEEE International Conference on Electronics, Circuits and Systems (ICECS), pp. 879–882 (2019)
15. Chahat, N., et al.: A compact UWB antenna for on-body applications. IEEE Trans. Antenn. Propag. 59(4), 1123–1131 (2011). https://doi.org/10.1109/tap.2011.2109361
16. Koohestani, M., et al.: A novel, low-profile, vertically-polarized UWB antenna for WBAN. IEEE Trans. Antenn. Propag. 62(4), 1888–1894 (2014). https://doi.org/10.1109/tap.2014.2298886
17. Lin, C.H., et al.: A compact planar inverted-F antenna for 2.45 GHz on-body communications. IEEE Trans. Antenn. Propag. 60(9), 4422–4426 (2012). https://doi.org/10.1109/tap.2012.2207038
18. Felício, J.M., et al.: Wrist-worn RFID antenna printed on additive manufactured flexible substrate. In: IEEE International Symposium on Antennas and Propagation and USNC-URSI Radio Science Meeting, pp. 83–84 (2019)
19. Colella, R., Chietera, F.P., Catarinucci, L.: Analysis of FDM and DLP 3D-printing technologies to prototype electromagnetic devices for RFID applications. Sensors. 21(3), 897 (2021). https://doi.org/10.3390/s21030897
20. Kimionis, J., et al.: 3D-printed origami packaging with inkjet-printed antennas for RF harvesting sensors. IEEE Trans. Microw. Theor. Tech. 63(12), 4521–4532 (2015). https://doi.org/10.1109/tmtt.2015.2494580
21. Tak, J., Kang, D.G., Choi, J.: A lightweight waveguide horn antenna made via 3D printing and conductive spray coating. Microw. Opt. Technol. Lett. 59(3), 727–729 (2017). https://doi.org/10.1002/mop.30374
22. Kate, J.T., Smit, G., Breedveld, P.: 3D-printed upper limb prostheses: a review. Disabil. Rehabil. Assist. Technol. 12(3), 300–314 (2017). https://doi.org/10.1080/17483107.2016.1253117
23. Aminzadeh, R., et al.: WBAN channel modeling for 900 MHz and 60 GHz communications. IEEE Trans. Antenn. Propag. 69(7), 4083–4092 (2021). https://doi.org/10.1109/tap.2020.3045498
24. Bae, J., et al.: The signal transmission mechanism on the surface of human body for body channel communication. IEEE Trans. Microw. Theor. Tech. 60(3), 582–593 (2012). https://doi.org/10.1109/tmtt.2011.2178857
25. Chahat, N., et al.: On-body propagation at 60 GHz. IEEE Trans. Antenn. Propag. 61(4), 1876–1888 (2013). https://doi.org/10.1109/tap.2013.2242034
26. Benarrouch, R., et al.: Capacitive body-coupled communication in the 400–500 MHz frequency band. In: Body Area Networks: Smart IoT and Big Data for Intelligent Health Management (BODYNETS), pp. 218–235 (2019)
27. Declercq, F., Rogier, H., Hertleer, C.: Permittivity and loss tangent characterization for garment antennas based on a new matrix-pencil two-line method. IEEE Trans. Antenn. Propag. 56(8), 2548–2554 (2008). https://doi.org/10.1109/tap.2008.927556
28. Balanis, C.A.: Antenna Theory: Analysis and Design, 3rd ed. John Wiley, Hoboken (2005)
29. McDowell, M.A., et al.: Anthropometric reference data for children and adults: United States, 2003–2006. Natl. Health Stat. Report. 10(1–45), 5 (2008)
30. Murdoch, A.H., Mathias, K.J., Smith, F.W.: Measurement of the bony anatomy of the humerus using magnetic resonance imaging. Proc. Inst. Mech. Eng. H. 216(1), 31–35 (2002). https://doi.org/10.1243/0954411021536252
31. Van Mulder, T.J.S., et al.: High frequency ultrasound to assess skin thickness in healthy adults. Vaccine. 35(14), 1810–1815 (2017). https://doi.org/10.1016/j.vaccine.2016.07.039
32. Jang, Y.W., Go, H.C., Lee, S.W.: A low profile post-type monopole antenna with a ring and four small posts. Microw. Opt. Technol. Lett. 52(4), 910–912 (2010). https://doi.org/10.1002/mop.25086
33. International Commission on Non-Ionizing Radiation Protection (ICNIRP): Guidelines for limiting exposure to electromagnetic fields (100 kHz to 300 GHz). Health Phys. 118(5), 483–524 (2020)
34. Felício, J.M., Fernandes, C.A., Costa, J.R.: Complex permittivity and anisotropy measurement of 3D-printed PLA at microwaves and millimeter-waves. In: 22nd International Conference on Applied Electromagnetics and Communications (ICECOM), pp. 1–6 (2016)
35. Reusens, E., et al.: Path loss models for wireless communication channel along arm and torso: measurements and simulations. In: IEEE Antennas and Propagation Society International Symposium, pp. 345–348 (2007)
36. Roelens, L., et al.: Path loss model for wireless narrowband communication above flat phantom. Electron. Lett. 42(1), 10–11 (2006). https://doi.org/10.1049/el:20063062
37. Chowdhury, H.R., Hassan, S., Ahmed, A.: Analysis of path loss characteristics in body area network for different physical structures. In: 9th International Conference on Electrical and Computer Engineering (ICECE), pp. 299–302 (2016)

How to cite this article: Proesmans, R., et al.: An on-body antenna for control of a wireless prosthesis in the 2.45 GHz industrial scientific & medical frequency band. IET Microw. Antennas Propag. 1–14 (2022). https://doi.org/10.1049/mia2.12309